Revision 2

Thermoelastic properties of natural zircon – Part I: Non-metamict zircon

Word Count: 6693

Marie Münchhalfen and Jürgen Schreuer

Ruhr-University Bochum, Institute of Geology, Mineralogy and Geophysics, Universitätsstr. 150, 44801 Bochum, Germany

Abstract

The thermoelastic properties and thermal expansion of natural single-crystal zircon without detectable radiation damage were determined in the temperature range between 100 K and 1650 K on five samples from Cambodia, Sri Lanka, and Tanzania. Up to about 1500 K, the results are in excellent agreement and fully reversible. The average adiabatic elastic stiffness coefficients at room temperature in GPa are c_{11} = 426.8(6), c_{12} = 68.1(4), c_{13} = 152.0(4), c_{33} = 490.8(9), c_{44} = 113.1(2) and c_{66} = 49.0(1). Polycrystalline averaging for the aggregate bulk and shear modulus (Voigt-Reuss-Hill average) yield K = 229.3(4) GPa and G = 109.3(1) GPa. From 293 K to 1573 K, the elastic stiffnesses soften almost linearly with the temperature coefficients in MPa/K: dc_{11}/dT = -45.36(7), dc_{12}/dT = -2.03(7), dc_{13}/dT = -9.59(7), dc_{33}/dT= -42.85(12), dc_{44}/dT = -9.60(3), and dc_{66}/dT = -2.19(1). Below room temperature, the behavior of the c_{ij} is non-linear, with decreasing absolute values of the temperature coefficients. Above about 1500 K, a temperature- and time-dependent irreversible elastic stiffening accompanied by an increasing ultrasound dissipation was observed in all samples. These anomalies are interpreted to be the consequence of increased dislocation densities.

Introduction

Zircon is a mineral of high geological relevance due to its widespread distribution in the continental crust, its resistance to chemical and physical degradation, and its tendency to concentrate trace elements, particularly lanthanides and actinides that allow for its use in age dating (e.g., Erwing, 2003).

Due to its favorable properties like high melting point and low thermal conductivity, zircon also finds practical industrial applications (Depmeier, 2009). For example, zircon-related synthetic materials such as xenotime-type $REPO_4$ have been explored as potential environmental barrier coating (Han et al., 2020). Another important field of application that has been considered is the long-time storage of radioactive fission products (Erwing et al., 1994) since zircon serves as an excellent matrix for immobilization by incorporating radioactive elements in the crystal structure. However, each radioactive decay causes local damage in the crystal structure, i.e., the total damage depends on the content of radiogenic elements and the age of the zircon crystal. The increasing degree of metamictization with increasing α-particle dosage is reflected by a decrease in density, an increase in cell parameters, and a severe change of elastic and optical properties, for example.

The first complete elastic data sets for non-metamict zircon at ambient conditions were published by Bhimasenachar and Venkataratnam (1955), and Ryzhova, Aleksandrov and Korobhova (1966). Later Özkan, Cartz, and Jamieson (1974) revised the data. The elastic behavior of zircon with and without radiation damage was studied by Özkan and Cartz (1974), Özkan, Cartz, and Jamieson (1974), and Özkan (1976), suggesting a systematic decrease of elastic stiffness coefficients with increasing degree of metamictization. Temperature derivatives of elastic coefficients of non-metamict zircon were determined between 295 K and 523 K (Özkan, Cartz, Fisher, 1975; Özkan, 2008) and more recently by Ehlers et al. (2022) between 293 K and 1172 K. An accurate knowledge of thermoelastic properties is relevant in geosciences since zircon is a common inclusion mineral with a promising potential for use in piezobarometry (e.g., Angel et al. 2015).

Therefore, our work aims to investigate in-situ temperature-dependent healing mechanisms of radioactively damaged zircon utilizing thermal expansion and thermoelastic properties. Both methods are well suited to studying changes in bond strength. For reference, this first publication focuses on the thermal expansion and thermoelastic behavior of non-metamict zircon.

EXPERIMENTAL

A. Sample description

Five gem-quality samples of natural zircon from three different localities were investigated (Figure 1 and Table 1). The colorless zircon I1 from Cambodia was reported to be a heated specimen. Zircon I2 from Sri Lanka was also likely thermally treated since the orange color was typical for heated gemstones and was retained even after experiments at high temperatures. The brownish zircon samples I3a-c from Tanzania, all taken from the same batch, were reportedly not subjected to any heat treatment.

B. Chemical and structural characterization

The chemical compositions were determined by electron probe microanalysis (EPMA) on polished samples of each crystal using an SXFiveFE electron microprobe from Cameca (Gennevilliers, France) with an accelerating potential of 20 keV and a current of 80 nA. The samples were analyzed for their SiO_2, ZrO_2, CaO, FeO, HfO_2, and UO_2 content by collecting data at 15 to 25 points distributed over each sample (standards: Si and Zr on $Zircon_{243}$, Ca on $Diopside_{210}$, Fe on $Fayalite_{212}$, Hf on S_{172}, U on U glass).

Single crystal diffraction (SXRD) data were collected on a four-circle kappa diffractometer (Xcalibur, Rigaku Oxford Diffraction) equipped with Sapphire2 CCD-detector using graphite-monochromatized MoKα radiation. The CrysAlisPro software package (version 1.171.36.24 by Rigaku Oxford Diffraction) was used for data reduction, including analytical absorption correction. Each structure was

solved with direct methods and refined employing a non-linear least-squares procedure as provided by the SHELX software package (Sheldrick, 2008). The composition as derived from EPMA was used in the refinement.

Powder X-ray diffraction (PXRD) data were recorded with a Siemens D5000 diffractometer in modified Debye-Scherrer geometry using Cu $K_{\alpha 1}$ radiation (λ = 1.54059 Å). The diffractometer was equipped with a curved germanium (111) primary monochromator and a Braun linear position-sensitive detector (2θ coverage = 6°). The powder samples were sealed in borosilicate glass capillaries (0.3 mm in diameter). Accurate cell parameters were determined with Fullprof software package (Rodríguez-Carvajal, 1993).

C. Sample preparation

All physical properties reported here are referred to a Cartesian reference system with axes $\mathbf{e_1}$, $\mathbf{e_2}$, and $\mathbf{e_3}$, which are parallel to the axes **a**, **b**, and **c** of the crystallographic reference system of tetragonal zircon (space group $I4_1/amd$).

Rectangular parallelepipeds suitable for resonant ultrasound spectroscopy and dilatometry were prepared from all raw crystals. The crystals were cut using a low-speed diamond saw (Isomet, Buehler) and polished on diamond discs (mesh 600 and 1200). Opposite faces were parallel to within ±1 μm, and deviations from the ideal orientation as controlled by Bragg and Laue diffraction techniques were less than 0.5°. Sample edge lengths l_i were between 2.546 mm and 6.691 mm, corresponding to sample volumes between 36.64 mm^3 and 100.91 mm^3. The aspect ratio of all cuboids is smaller than 2. The geometric densities $\rho_{geo} = m/l_1 l_2 l_3$ were calculated from sample mass m and edge lengths l_i (Table 1). Additionally, for the investigation of thermal expansion, thick plates with parallel faces perpendicular to [001] were fabricated from zircons I1 and I2 and with parallel faces perpendicular to [100] from zircon I2. The thicknesses of these samples were in the range of 3.250 mm to 6.794 mm.

100

101 **D. Elastic coefficients**

102 The adiabatic elastic properties were studied with resonant ultrasound spectroscopy (RUS) (e.g.,
103 Migliori, 1997; Leisure, 1997). A frequency response analyzer FRA5087 from NF corporation was
104 employed for signal generation and detection at ambient temperatures. In order to approximate the
105 boundary conditions of a freely vibrating sample, the rectangular parallelepipeds were gently clamped
106 at opposite corners between two horizontally arranged ultrasonic transducers, keeping the mechanical
107 load on the sample below about 50 mN. Four resonance spectra on each sample were collected in the
108 frequency range between 100 kHz and 2000 kHz, with the sample mounted in different orientations.
109 The six independent elastic stiffnesses c_{ij} of each sample were derived by a non-linear least-squares
110 procedure from the measured frequencies of 60 eigenmodes, corresponding to a 10-fold
111 overdetermination of the system of non-linear equations. In order to minimize truncation effects, 2925
112 normalized Legendre polynomials were used to approximate each component ξ_i of the displacement
113 vector (program rusref, version V01.13.01).
114 For RUS measurements at non-ambient temperatures, two different devices built in-house were used
115 for data collection; one operating in the temperature range 103 K – 673 K and one covering the range
116 from room temperature to 1773 K. For both setups, the frequency response analyzer (FRA5087) was
117 employed in combination with a high-speed bipolar amplifier BA4825 by NF corporation for signal
118 generation and detection. The samples were clamped at opposite corners between two horizontally
119 arranged ultrasonic transducer rods made of corundum ceramic. A liquid nitrogen cooling system and a
120 furnace with a resistance heater were employed in the low-temperature measurements. The temperature
121 was controlled by a Eurotherm 2704 and a system power supply of type 6675A from Agilent. All low-
122 temperature experiments were carried out in He purge gas atmosphere at a flow rate of about 2 l/h. The
123 high-temperature setup only differs concerning the type of furnace used. Here type S thermocouples
124 and a furnace with SiC heating element were employed, and the experiments were carried out in the air.

This is the peer-reviewed, final accepted version for American Mineralogist, published by the Mineralogical Society of America.
The published version is subject to change. Cite as Authors (Year) Title. American Mineralogist, in press.
DOI: https://doi.org/10.2138/am-2023-8986. http://www.minsocam.org/

All samples were first measured with the low-temperature setup between 103 K and 323 K, collecting resonance spectra every 20 K. The high-temperature measurement started at 303 K, with spectra collected every 10 K or 20 K. Heating/cooling rates between the temperature steps were 2 K/min. The maximum temperature was 1053 K for sample I, 1473 K for samples I2 and I3c, 1573 K for sample I3c, and 1673 K for sample I3a. For the accurate determination of the c_{ij}, experimental data of thermally induced strains were used to correct the sample dimensions and density for thermal expansion effects (cf. section E).

Additionally, we collected 20 subsequent resonance spectra at 1573 K, each run lasting about 20 min, on sample I3a.2 having no defined shape or orientation to study the time-dependence of eigenfrequencies and ultrasound attenuation at a constant temperature. For quantification of the ultrasound attenuation the inverse quality factor of selected resonances defined by

$$Q^{-1} = \frac{\Delta f}{f_0} \quad (1)$$

with resonance frequency f_0 and its full-width at half-maximum Δf was determined by fitting modified split Lorentzian functions to resonance peaks.

E. Thermal expansion

The coefficients of thermal expansion were derived from temperature-induced strains as determined by a commercial inductive gauge dilatometer type DIL402C from Netzsch (Selb, Germany). Two different experimental setups covered the temperature range from 100 K to 1700 K. The low-temperature setup (100 K – 700 K) consisted of a sample holder made of fused silica, thermocouples of type E, a liquid nitrogen cooling system, and a furnace with a resistance heater. The high-temperature setup (295 K – 1700 K) was equipped with a sample holder made of corundum ceramic, type S thermocouples, and a furnace with a SiC heating element. The dilatometer was first calibrated with standard rod-shaped

149 samples of different lengths made of fused silica and corundum ceramic, both supplied by Netzsch. All
150 experiments were carried out applying heating/cooling rates of 2 K min^{-1} in air (high-temperature
151 setup) and, respectively, in He purge gas atmosphere at a flow rate of about 2 l/h (low-temperature
152 setup).
153 The strain was measured on samples exclusively fabricated for DIL measurements that were not
154 previously subjected to heating experiments of samples I1, I2, and I3a in [001] and for I2 additionally
155 in [100]. The measurements covered a temperature range between 100 K and 1673 K.
156 The strain was also investigated on sample I1 which had been previously heated up to 1053 K in RUS
157 experiments.
158

159 **RESULTS**

160

161 **A. Chemical and structural composition**

162 The chemical compositions, determined with electron microprobe analysis, are listed in Table 1.
163 Only HfO_2 was found in significant quantities (see. Table 1). The contents of UO_2, CaO, and FeO were
164 within error limits and were, therefore, neglected. The samples yielded no hint of any zoning regarding
165 the distribution of the investigated elements. Based on ionic radii (Shannon, 1976) Hf was presumed to
166 substitute Zr, and the density determined from powder X-ray diffraction ρ_x was corrected accordingly
167 (Table 1). Cell parameters differ by less than 0.0004 Å for all samples. Under experimental error, no
168 systematic difference between X-ray and geometric density could be detected. Gemstones I1 and I2 are
169 thermally treated zircons, i.e., possible radiation defects that were originally present have probably
170 largely healed (Erwing, 2003). Therefore, the only very small differences in density and lattice
171 parameters of all samples suggest no relevant radiation defects.

172

This is the peer-reviewed, final accepted version for American Mineralogist, published by the Mineralogical Society of America.
The published version is subject to change. Cite as Authors (Year) Title. American Mineralogist, in press.
DOI: https://doi.org/10.2138/am-2023-8986. http://www.minsocam.org/

173 **B. Elastic coefficients at ambient temperatures**

174 Elastic stiffness coefficients c_{ij} of samples at ambient temperatures are listed in Table 2. The R-values
175 defined as

$$R = \frac{\sum \left(\omega_{ci}^2 - \omega_{oi}^2\right)}{\sum \omega_{oi}^2} \quad (2)$$

176

177 with ω_{oi} observed circular frequencies and ω_{ci} calculated ones are small (Table 2), indicating the high
178 quality of the refinements. The uncertainties of the c_{ij} of the five samples represented by the standard
179 deviations derived from the covariance matrix of the fully converged least-squares refinement are
180 smaller than 0.13 % for the c_{ii} and 1.31% and 0.18% for the transverse interaction coefficients c_{12} and
181 c_{13}, respectively. There is no discernible difference in the elastic behavior between heated samples I1
182 and I2 and non-heated samples I3a-c. The coefficients are excellently reproducible, with variations of
183 less than 0.5% for the c_{ii} ± and 1.5% and 0.6% for the transverse interaction coefficients c_{12} and c_{13},
184 respectively. for all samples.
185 While older data by Ryzhova et al. (1966) (revised by Özkan et al. 1974) differ significantly, the c_{ij}
186 values reported by Özkan and Cartz (1974) determined with the ultrasonic phase comparison method
187 agree well for their higher-density zircons (Table 3) and are slightly off for the lower-density
188 specimens. The shear stiffness coefficients are generally in good agreement with the literature data.
189 However, the longitudinal and transverse interaction coefficients of non-metamict zircon by Ehlers et
190 al. (2022), also determined with resonant ultrasound spectroscopy, agree less, with their c_{11} and c_{33}
191 being higher by 1.1-2%, and c_{12} and c_{13} even higher by 5.3-10.6 %, despite a lower reported density
192 (Table 2). The authors already noted these differences in comparison to the results of Özkan and Cartz
193 (1974). They attributed this pattern of deviation to a systematic error in their data set caused by the
194 small dimensions of their sample. However, this argument is not valid because the relative contribution
195 of the individual c_{ij} to the eigenmodes does not change with the size but only with the aspect ratio of
196 the sample. Moreover, the dimensions of the sample used by Ehlers and co-workers are within the

range of our samples (Table 1) and we do not observe such a systematic deviation. Although the cause is still unclear, Ehlers et al. (2022) have corrected for the deviations by introducing appropriate scale factors in their fit of a third-order Birch-Murnaghan equation of state. The resulting adiabatic Reuss bulk modulus of 225.0(1.2) GPa at room temperature agrees within one standard deviation with the averaged value 226.5(4) GPa obtained in this work (Table 3).

C. Elastic coefficients at non-ambient temperatures

Thermoelastic properties of non-metamict zircon samples are also well reproducible for all samples (Figure 2). Between 52 and 72 eigenfrequencies were analyzed for each temperature step, yielding *R*-values between 0.4 to 1.9 ‰. *R*-values significantly increase at temperatures above about 1400 K. Elastic coefficients c_{ij} could be determined up to 1573 K. No offset of elastic stiffnesses between heating and cooling has been observed if the samples were subjected to temperatures up to a maximum of 1473 K. The colorless sample I1 and orange sample I2 did not change their optical appearance after heating, supporting the presumption that the raw material had already been heated. The brown samples I3a-c lost their color after heating (sample I3a after first heating to 1053 K). No effect is visible in the RUS spectra that could be correlated with the color change. The color is likely a result of a comparably small number of isolated point defects that function as color centers.

The elastic stiffness coefficients $c_{ij}(T)$ decrease approximately linearly between ambient temperatures and 1573 K. Below ambient temperatures, the temperature dependence of the c_{ij} Debye deviates from linear behavior. For comparison with previously published adiabatic data, $c_{ij}(T)$ were linearly fitted between 293 K and 1573 K (Table 4). Due to the excellent reproducibility, all data points of all samples were fitted together. Thermoelastic data for zircon from Özkan (2008) agree well with our results (Figure 2). Although the individual c_{ij} reported by Ehlers et al. (2022) are larger, the temperature dependence, however, is similar. The elastic stiffnesses decrease with temperature with no

significant change of the elastic anisotropy as indicated by the ratio of the maximum and minimum of longitudinal elastic stiffness $c'_{11}{}^{max}$/ $c'_{11}{}^{min}$ changing only from 1.656 to 1.659 between 295 K and 1473 K. Data sets including c_{ij}, bulk and shear moduli of each sample at each investigated temperature are available as supplementary material.

From about 1500 K, the eigenfrequencies start shifting to higher frequencies, which is accompanied by an increase in ultrasound attenuation, indicating an elastic stiffening of the samples with increasing temperature (Figure 3). On samples I2 and I3c, heated to 1473 K, these effects are barely noticeable, whereas, on samples I3b and I3a, heated to higher temperatures, these effects are more pronounced. All samples heated over 1473 K cracked shortly after cooling to room temperature started, making further quantitative data analysis impossible. In order to get insight into the kinetics of the processes at high temperatures, a qualitative time-depended series of experiments was conducted at T = 1573 K on a second sample cut from I3a (I3a.2). As shown in Figure 4, the eigenfrequencies of the sample shifted monotonously by about 3.2 kHz over 7 hours, accompanied by an increase in ultrasound attenuation. The increase of the eigenfrequencies flattens with time, indicating a potential saturation of the observed effect.

In Figure 5 adiabatic bulk moduli (Voigt-Reuss-Hill average) obtained in this work are compared to values from the literature for non-metamict zircon. The comparison includes data from DFT calculations as well as experiments. In cases were c_{ij} were available, the Voigt-Reuss-Hill average was calculated. Bulk moduli for Reuss case are only included in temperature-dependent data.

Values for the bulk modulus calculated in the athermal limit scatter significantly. DFT calculations for the bulk modulus at 0 K range between 186.6 GPa and 251 GPa (Bannikov et al., 2011, Chaplot et al., 2006, Du et al., 2012, Dutta & Mandal, 2012, Mittal et al., 2000, Terki et al., 2005, Xiang et al., 2015). Although there is no clear separation, the generalized gradient approximation (GGA) tends to deliver lower values (range 186.6 – 231.8 GPa), while the local density approximation (LDA) gives, on average higher values (range 224.1 – 251 GPa).

This is the peer-reviewed, final accepted version for American Mineralogist, published by the Mineralogical Society of America.
The published version is subject to change. Cite as Authors (Year) Title. American Mineralogist, in press.
DOI: https://doi.org/10.2138/am-2023-8986. http://www.minsocam.org/

The experimental data for the bulk modulus at ambient temperatures (Ryzhova et al. 1966, Özkan and Cartz 1974, Özkan et al., 1974, and Ehlers, et al., 2022) scatter less (range 206 – 228 GPa), however, still significantly more than the experimental bulk modulus at room temperature obtained in this work (range 228.8 – 229.9 GPa).

Since no experimental data at 0 K is available, the temperature-dependent adiabatic bulk modulus (VRH) of all obtained data from this work were approximated with an equation proposed by Varshni (1970) based on a single-frequency Einstein model

$$K(T) = K^0 - \frac{s}{e^{t/T} - 1} \quad (3)$$

where K^0 is the bulk modulus at 0 K, and s and t are parameters describing the evolution of K with temperature T. The resulting fit parameters were K^0 = 232.3(1) GPa, s = 6.6(5) GPa, and t = 328(24) K. These values are in best agreement with the GGA-based calculation by Dutta and Mandal (2012). The experimental data by Ehlers et al. (2022) yielded a slightly higher value, while the bulk modulus from Özkan et al. (1975) is slightly lower. The data, however, fit very well with newer data from Özkan (2008) that were estimated based on earlier experimental work. Taking into account only the slope , all published experimental *K(T)* are in reasonable agreement with our data.

Calculations of $K(T)$ were performed by Terki et al. (2005), Du et al. (2012), and Chiker et al. (2016) using DFT in combination with the quasi-harmonic Debye model. Since the calculations from Du et al. (2012), and Chiker et al. (2016) should deliver the bulk modulus for the Reuss case, our data was approximated with the Varshni fit for the Reuss modulus as well (Fig. 5).

While the difference between isothermal and adiabatic approximation is significant, the calculated slopes of $K(T)$ differ even stronger from each other, with no good agreement with any experimental data.

D. Thermal expansion

The experimental thermal strain is reproducible on heated (for example, in previous RUS experiments) and unheated samples (Figure 6). Samples I1 and I2 were heat treated prior to any experiments; nevertheless, sample I3a, with no previous heat treatments, delivered comparable data. For comparison to literature data, strains were calculated from temperature-depended cell parameters reported by Subbarao and Gokhale (1968) (X-ray diffraction), Bayer (1971) (X-ray diffraction), Mursic et al. (1992) (neutron powder diffraction), Chaplot et al. (2002) (synchrotron X-ray diffraction) and Austin (1931), who determined the macroscopic thermal expansion using the Pulfrich-Fizeau interference method. All literature data agree reasonably well, with Austin (1931) and Mursic et al. (1992) providing the best match to our data. Mursic et al. (1992), however, observed an anomaly characterized by decreasing thermal expansion starting at around 1100 K on synthetic zircon that was not reproducible in our measurements on natural zircon. Since the thermal expansion data are well reproducible on all investigated samples, the data points, excluding devations at high temperatures, were fitted with an Einstein model (Figure 7), for the strains ε_{11} and ε_{33}, respectively. Based on the phonon density of states calculated by Chaplot et al. (2006) a two-frequency model was chosen:

$$\varepsilon_{ij}(T) = \varepsilon_{ij}^{0} + \alpha_{ij}^{h1} \frac{\Theta_E^1}{-1 + e^{\frac{\Theta_E^1}{T}}} + \alpha_{ij}^{h2} \frac{\Theta_E^2}{-1 + e^{\frac{\Theta_E^2}{T}}} \quad (4)$$

Additionally, the curves were fitted with polynomials $\varepsilon_{ij} = \varepsilon_0 + \alpha_{ij}(T - T_0) + \beta_{ij}(T - T_0)^2 + \gamma_{ij}(T - T_0)^3 + \delta_{ij}(T - T_0)^4$ with $T_0 = 295$ K in order to best approximate the measured strain curves. Fit parameters of both approaches are listed in Table 5.

While the Einstein model describes the thermal expansion very well below 1500 K, significant deviations are observed at higher temperatures (Figure 7), i.e., in the same temperature range where

anomalies in the evolution of the resonance frequencies occur (see section IIID). Data files including thermal strain and thermal expansion for all samples can be found in the supplement.

DISCUSSION

The zircon structure consists of ZrO_8 dodecahedra and SiO_4 tetrahedra (Figure 8). For each polyhedron, half of the bonds are arranged in the plane perpendicular to [100], while the other half is arranged in the plane perpendicular to [010] due to symmetry. The bond valences (Brown, 2006), as a measure of bond strength, of the Si – O bonds are roughly twice as high as those of the Zr – O bond. Hence, the SiO_4 tetrahedra can be considered rigid units of the structure. Each ZrO_8 dodecahedron is edge-connected to two SiO_4 tetrahedra and four other ZrO_8 dodecahedra, with no direct connection between the SiO_4 tetrahedra. Therefore, the structure can be described as consisting of intersecting ZrO_8 chains along <100>, which are additionally linked by SiO_4 tetrahedra along <001> (Figure 8a).

The longitudinal elastic stiffness is almost isotropic in the {100} planes (Figure 8a), with a slightly higher value along [001]. Any compression along the tetragonal axis would reduce the Zr—O bond length or change the bond angles of both types of cation polyhedra. Slightly more favorable is the compression in [100], which can be compensated by changes in Zr—O bond length without geometrical changes in the SiO_4 tetrahedra. Within the (001) plane, the elastic anisotropy is more pronounced (Figure 8b), with maxima along <100> and minima along <110>. The edge-connections between SiO_4 tetrahedra and ZrO_8 dodecahedra are exclusively orientated in <100>, while none of these bonds have a contribution in <110>, making the latter an elastic softer direction. A compression along <110> can be obtained by a change of bond angles only.

The absolute value of the maximum longitudinal elastic stiffness in <001> decreases more than the one of the minimal stiffness in <110> (e.g., between 303 K and 1473 K by 51 GPa compared to 32 GPa); hence elastic anisotropy remains nearly constant in the entire investigated temperature range (Figure 9).

This is the peer-reviewed, final accepted version for American Mineralogist, published by the Mineralogical Society of America.
The published version is subject to change. Cite as Authors (Year) Title. American Mineralogist, in press.
DOI: https://doi.org/10.2138/am-2023-8986. http://www.minsocam.org/

In contrast to the elastic behavior, a pronounced anisotropy characterizes the thermal expansion tensor with the maximum along the tetragonal axis (Figure 10). According to Hazen and Finger (1979), thermal expansion is mainly influenced by the ZrO_8 dodecahedra. Since those are edge-connected to the more rigid SiO_4 tetrahedra in the (001) plane, the contribution to thermal expansion is larger along [001]. Another contribution is correlated to the change in bond angles of the SiO_4 tetrahedra. At ambient temperature, the bond angles in the SiO_4 tetrahedra are not ideal, with angles between 97° and 116°. Mursic et al. (1992) observed an increase in the smaller bond angle with temperature, which necessarily leads to a simultaneous decrease of the larger angle. Thus the SiO_4 tetrahedra become more idealized at higher temperatures. Oxygen atoms of smaller bond angles are edge-connected to the ZrO_8 dodecahedra. As a result of the change in bond angles, the ZrO_8 chains move closer to one another, leading to a negative contribution to the thermal expansion in the (001) plane.

In zircon the anisotropy of the thermal expansion and linear compressibility, as expressed by the 2nd rank tensors (α_{ij}) and (β_{ij}), causes the corresponding longitudinal effects $\varepsilon_{11}{}^{T'} = u_{1i}u_{1j}\varepsilon_{ij}{}^{T} = u_{1i}u_{1j}\alpha_{ij}\Delta T$ and $\varepsilon_{11}{}^{P'} = -u_{1i}u_{1j}\beta_{ij}\Delta P$ to change with the direction $\mathbf{u} = u_{1i}\mathbf{e}_i$ in the crystal (u_{1i} are direction cosine). ε_{ij} denote the components of the strain tensor, T and P are temperature and pressure, respectively, and the Einstein sum convention applies. The anisotropy is illustrated in Figure 11, where the hydrostatic pressures

$$\Delta P_e = \frac{\varepsilon_{11}^{T\,\prime}}{u_{1i}u_{1j}\beta_{ij}} \quad (5)$$

required to compensate for the temperature-induced strains $\varepsilon_{11}{}^{T}$, $\varepsilon_{33}{}^{T}$ and $\varepsilon_{11}{}^{T} + \varepsilon_{22}{}^{T} + \varepsilon_{33}{}^{T} = \Delta V/V$ starting from room temperature ($\Delta T = 0$) are shown. ΔP_e were calculated using experimental thermal strains and adiabatic elastic stiffnesses $c_{ij}(T)$ obtained in this work (see supplementary data files), but neglecting any pressure dependence. The reference surface in Figure 11 exemplifies the spatial variation of ΔP_e at 1273 K. As outlined by Angel et al. (2019), the required pressure is maximal along

the stiffest direction [001] and minimal in the plane perpendicular to the tetragonal axis. A more general measure of the anisotropy is therefore provided by

$$\frac{\alpha_{33}-\beta_{11}}{\beta_{33}-\alpha_{11}} \quad (6).$$

Above room temperature this factor varies only slightly between about 3.0 and 3.6. The anisotropy of ΔP_e will have two consequences for the stress fields in and around zircon inclusions trapped in other minerals. First, the anisotropy of the stress field in the host around the inclusion will be increased relative to that expected for an isotropic inclusion with the same bulk properties as zircon. Second, in stiff hosts, the zircon inclusions will themselves exhibit significant internal non-hydrostatic stress.

The situation is unclear when comparing the irreversible elastic anomalies observed above about 1500 K to unusual effects at high temperatures described in the literature. On severely radiation-damaged zircon Farges (1994) observed the appearance of monoclinic zirconia at temperatures above about1573 K, while Vance & Boland (1975) reported the disappearance of the ZrO_2 phase after annealing to 1573 K. Experiments on high purity zircon revealed the onset of thermal dissociation to form ZrO_2 and SiO_2 at temperatures not lower than 1800 K (e.g., Anseau et al., 1976; Kaiser et al., 2008). On the other hand, an increase of dislocation loops was observed by Bursil and MacLaren (1966) when annealing severely radiation damaged samples at temperatures above about 1523 K. According to Granato and Lücke (1956a, 1956b) an increase in dislocation density is correlated with an increase in ultrasound attenuation. Another consequence of increasing dislocation density would be elastic stiffening due to increasing internal stresses, which matches our observations. Moreover, as local inhomogeneities pin the dislocations, the resulting inhomogeneous stress fields reinforced by thermal expansion effects might be responsible for the cracking of the samples on cooling.

Implications

The temperature-dependent elastic properties of non-metamict zircon were studied on five samples of different origins by resonant ultrasound spectroscopy extending the knowledge of the elastic behavior of zircon to lower and higher temperatures compared to previous work. Our results at room temperature are in reasonable agreement with literature data on non-metamict zircon investigated using different techniques. The excellent reproducibility and reversibility of the thermoelastic properties in the temperature range of 100 K to 1500 K suggest a high reliability of the adiabatic elastic stiffnesses obtained in this work. Moreover, up to 1500 K the behavior of the elastic stiffnesses and of the thermal expansion coefficients can be well explained by individual vibrations of the atoms in their local potentials. Thus, the thermoelastic data can be used as reference data to identify and quantify pathological behavior of other zircon crystals. The new data also allow for improved fits of equations of state. However, concerning applications in elastic barometry, the significantly anisotropic elastic response of zircon on temperature and pressure changes, respectively, represents an additional challenge. Above about 1500 K and thus well below the onset of thermal decomposition at 1800 K, an irreversible elastic stiffening occurs, that could be related to an increase in dislocation density due to internal stresses.

Acknowledgment

The authors would like to thank Eckehard Petsch (Idar-Oberstein, Germany) for donating the zircons from Tanzania (samples I3a-c) and Manfred Burianek (Cologne, Germany) for providing the zircon from Sri Lanka. The gemstone from Cambodia was taken from the private collection of one of the authors.

References

Angel, R.J., Nimis, P., Mazzucchelli, M., Alvaro, M. and Nestola, F. (2015) How large are departures from lithostatic pressure? Constraints from host inclusion elasticity. Journal of Metamorphic Geology, 33, 801-813.

Angel, R.J., Miozzi, F. And Alvaro, M. (2019) Limits to the validity of thermal-pressure euqations of state. Minerals, 9, 562/1-11.

Anseau, M.R., Biloque, J.P. and Fierens, P. (1976) Some studies on the thermal solid state stability of zircon. Journal of Materials Science, 11, 578–582.

Austin, J.B. (1931) The thermal expansion of some refractory oxides. Journal of the American Ceramic Society, 14, 795-810.

Bannikov,V.V., Shein, I. R., Ivanovskii, A. L. (2012) Mechanical properties and electronic structure of zircon: Ab Inito FLAPW-GGA Calculations. Inorganic Materials: Applied Research, 3, 7–10.

Bayer, G. (1971) Thermal expansion ABO_4-compounds with zircon- and scheelite structures. Journal of less-common metals, 26, 255-262.

Bhimasenachar, J. and Venkataratnam G. (1955) Elastic constants of zircon.
The Journal of the Acoustical Society of America, 27, 922–925.

Brown, I.D. (2006) The chemical bond in inorganic chemistry: The bond valence
model. IUCr monographs on crystallography. Oxford University Press.

Bursill, L.A. and McLaren, A.C. (1966) Transmission electron microscope study of natural radiation damage in zircon ($ZrSiO_4$). Physica status solidi (b), 13, 331–343.

Chaplot, S.L., Mittal, R., Busetto, E., Lausi, A. (2002) Thermal expansion in zircon and almandine: Synchrotron x-ray diffraction and lattice dynamical study. Physical Review B, 66, 064302.

Chaplot, S.L., Pintschovius, L., Choudhury, N., Mittal, R. (2006) Phonon dispersion relations, phase transitions, and thermodynamic properties of $ZrSiO_4$: Inelastic neutron scattering experiments, shell model, and first-principles calculations. Physical review B 73, 094308.

Chiker, F., Boukabrine, F., Khachai, H. et al. (2016) Investigating the structural, thermal, and electronic properties of the zircon-type $ZrSiO_4$, $ZrGeO_4$ and $HfSiO_4$ compounds. Journal of Electronic Materials, 45, 5811–5821.

Depmeier, W. (2009) Minerals as advanced materials. Crystal Research and Technology, 44, 1122-1130.

Du, J., Devanathan, R., Corrales, L.R., Weber, W.J. (2012) First-principles calculations of the electronic structure, phase transition andproperties of $ZrSiO_4$ polymorphs. Computational and Theoretical Chemistry, 987, 62–70.

Dutta, R., Mandal, N. (2012) Effects of pressure on the elasticity and stability of zircon ($ZrSiO_4$): First-principle investigations. Computational Materials Science, 54,157–164.

Ehlers, A.M., Zaffiro, G., Angel, R.J., Boffa-Ballaran, T. Carpenter, M.A., Alvaro, M.and Ross, N.L. (2022) Thermoelastic properties of zircon: Implications for geothermobarometry. American Mineralogist, 107, 74-81.

Ewing, R.C. (1994) The metamict state: 1993 - the centennial.
Nuclear Instruments and Methods in Physics Research Section B, 91, 22-29.

Ewing, R.C., Meldrum, A., Wang, L.M., Weber, W.J., Corrales, L.R. (2003) Radiation effects in zircon. Reviews in Mineralogy and Geochemistry, 53, 387–425.

Farges, F. (1994) The structure of metamict zircon: A temperature-dependent EXAFS study. Physics and Chemistry of Minerals, 20, 504-514.

Granato, A., Lücke, K. (1956a) Theory of mechanical damping due to dislocations. Journal of Applied Physics 27, 583- 593.

Granato, A., Lücke, K. (1956b) Application of dislocation theory to
internal friction phenomena at high frequencies. Journal of Applied Physics 27, 789- 805.

Han, J., Wang, Y., Liu, R. Wan, F. (2020) Theoretical and experimental investigation of xenotime-type rare earth phosphate $REPO_4$, (RE = Lu, Yb, Er, Y and Sc) for potential environmental barrier coating applications. Scientific Reports 10, 13681.

Hazen, R.M., Finger, L.W. (1979) Crystal structure and compressibility of zircon at high pressure. American Mineralogist, 64, 196-201.

Kaiser, A., Lobert, M., Telle, R. (2008) Thermal stability of zircon ($ZrSiO_4$).
Journal of the European Ceramic Society, 28, 2199-2211.

Leisure, R.G. and Willis, F.A. (1997) Resonant ultrasound spectroscopy. Journal of Physics: Condensed Matter, 9, 6001–6029.

Migliori, A. and Sarrao. J. (1997) Resonant ultrasound spectroscopy. John Wiley & Sons, New York.

Mittal, R., Chaplot, S.L., Parthasarathy, R., Bull, M.J., Harris, M.J. (2000) Lattice dynamics calculations and phonon dispersion measurements of zircon, ZrSiO4. Pysical Review B, 62, 12089-12094.

Mursic, Z., Vogt, T., and Frey, F. (1992) High-temperature neutron powder diffraction study of $ZrSiO_4$ up to 1900 K. Acta Crystallographica, B48, 584-590.

Özkan, H., (1976) Effect of nuclear radiation on the elastic moduli of zircon. Journal of Applied Physics 47, 4772-4779.

Özkan, H., (2008) Correlations of the temperature and pressure dependencies of the elastic constants of zircon. Journal of the European Ceramic Society, 28, 3091–3095

Özkan, H. and Cartz, L. (1974) Anisotropic thermophysical properties of zircons. AIP Conference Proceedings, 17, 21–33.

Özkan, H., Cartz, L., and Jamieson, J.C. (1974) Elastic constants of nonmetamict zirconium silicate. Journal of Applied Physics 45, 556–562.

Özkan, H., Cartz, L., and Fisher, E.S. (1975) Temperature dependence of the elastic constants of zircon. Revue internationale des hautes temperatures et des refractaires, 12, 52–57.

Rodríguez-Carvajal, J. (1993) Recent advances in magnetic structure determination by neutron powder diffraction. Physica B: Condensed Matter, 192, 55–69

Ryzhova, T.V., Aleksandrov, K.S., and Korobhova, V.M. (1966) The elastic properties of rock-forming minerals V: additional data on sillicates. Izvestiya, Physics of the Solid Earth, 63.

Shannon, R.D. (1976) Revised effective ionic radii and systematic studies of interatomic distances in halides and chalcogenides. Acta Crystallographica A, 32, 751–767.

Sheldrick, G.M. (2008) A short history of SHELX. Acta Crystallographica A 64, 112–122.Subbarao, E.C. and Gokhale, K.V.G.K. (1968) Thermal Expansion of Zircon. Japanese Journal of Applied Physics, 7, 1126.

Subbarao, E.C. and Gokhale, K.V.G.K. (1968) Thermal expansion of zircon. Japanese Journal of Applied Physics, 7, 1126.

Terki, R., Bertrand,, G., Aourag, H. (2005) Full potential investigations of structural and electronic properties of $ZrSiO_4$. Microelectronic Engineering, 81, 514–523.

Vance, E.R. and Boland, J.N. (1975) Fission fragment damage in zircon. Radiation Effects, 26, 135-139.

Varshni, Y. P. (1970) Temperature dependence of the elastic constants. Physical Review B, 2, 3952–3958.

Xiang, H., Feng, Z., Li, Z., Zhou, Y. (2015) Theoretical investigations on mechanical and thermal properties of $MSiO_4$ (M = Zr, Hf). Journal of Materials Research, 3, 2030-2039.

This is the peer-reviewed, final accepted version for American Mineralogist, published by the Mineralogical Society of America.
The published version is subject to change. Cite as Authors (Year) Title. American Mineralogist, in press.
DOI: https://doi.org/10.2138/am-2023-8986. http://www.minsocam.org/

532

533 **TABLE 1.** Chemical composition, lattice parameters and density of zircon crystals. Additionally, the
534 edge lengths of oriented cuboidal samples used for RUS experiments are given.

Zircon		I1	I2	I3a	I3b	I3c
Treatment		heated	heated*	no	no	no
Chemical composition mol%	SiO_2	50.28(8)	49.92(21)	50.04(10)	50.27(16)	50.07(18)
	ZrO_2	49.35(14)	49.70(17)	49.53(10)	49.21(15)	49.45(18)
	HfO_2	0.37(1)	0.38(1)	0.43(1)	0.52(1)	0.48(1)
Lattice parameters	a (Å)	6.60367(7)	6.60373(8)	6.60337(8)	6.60356(4)	6.60334(5)
	c (Å)	5.97875(14)	5.97902(13)	5.97872(13)	5.97896(8)	5.97886(9)
Density	ρ_x (gcm^{-3})	4.686(9)	4.687(13)	4.690(7)	4.693(11)	4.692(13)
	ρ_{geo} (gcm^{-3})	4.677(3)	4.676(1)	4.677(4)	4.675(2)	4.676(1)
Sample dimensions	l_1 (mm)	4.365(1)	3.570(1)	3.873(1)	3.079(1)	3.683(1)
	l_2 (mm)	3.455(1)	3.120(1)	3.358(1)	4.675(1)	3.820(1)
	l_3 (mm)	6.691(1)	4.169(1)	5.403(1)	2.545(1)	4.042(1)

535 * heat treatment was presumed based on specific properties of the sample (see section A).

536

TABLE 2. Adiabatic elastic stiffnesses c_{ij} of non-metamict zircon at room temperature obtained in this work on as-prepared samples using the RUS method. Numbers in parentheses of c_{ij} are the standard deviations derived from the covariance matrix of the fully converged refinement. ρ_{geo} geometrical density derived from sample mass and dimensions, R final residual, Δf_{av} and Δf_{max} average and maximum difference $|f_{calc}-f_{obs}|$ between calculated and observed frequencies.

Zircon	I1	I2	I3a	I3b	I3c
c_{11} (GPa)	426.6(3)	427.5(2)	426.0(2)	426.9(2)	427.0(3)
c_{12} (GPa)	67.9(9)	68.5(6)	67.8(6)	68.6(8)	67.6(6)
c_{13} (GPa)	151.8(3)	152.7(2)	151.8(2)	151.9(2)	152.0(2)
c_{33} (GPa)	490.5(6)	492.0(5)	489.8(6)	490.4(3)	491.3(5)
c_{44} (GPa)	113.3(1)	113.5(1)	113.1(1)	113.3(1)	113.5(1)
c_{66} (GPa)	48.9(1)	49.1(1)	49.0(1)	49.0(1)	49.0(1)
$R\cdot1000$	0.37	0.61	0.67	0.81	1.08
Δf_{av} (kHz)	0.19	0.44	0.40	0.61	0.71
Δf_{max} (kHz)	0.94	1.6	1.23	1.93	2.79

537

This is the peer-reviewed, final accepted version for American Mineralogist, published by the Mineralogical Society of America.
The published version is subject to change. Cite as Authors (Year) Title. American Mineralogist, in press.
DOI: https://doi.org/10.2138/am-2023-8986. http://www.minsocam.org/

TABLE 3. Comparison of room temperature adiabatic elastic properties of non-metamict zircon with literature data. c_{ij} elastic stiffness coefficients, ρ density, c_{ij}^{iso} aggregate elastic stiffnesses (VRH-average), K bulk modulus (VRH-average), K_V Voigt modulus, K_R Reuss modulus, $c_{11}{}'^{max}/c_{11}{}'^{min}$ ratio of maximum and minimum of longitudinal elastic stiffness. Methods: PE - pulse echo, PSP - pulse superposition, RUS – resonant ultrasound spectroscopy.

Reference	Ryzhova et al., 1966 *	Özkan et al., 1974	Özkan et al., 1974	Ehlers et al., 2022	This work (average)
Method	PE	PSP	PSP	RUS	RUS
ρ (gcm^{-3})	4.70	4.649	4.675	4.661	4.676(1)
c_{11} (GPa)	330.1	422.9	424.4	431.4(2.9)	426.8(6)
c_{12} (GPa)	107.5	71.4	69.2	75.3(3.1)	68.1(4)
c_{13} (GPa)	154.2	148.7	150.2	160(4.3)	152.0(4)
c_{33} (GPa)	380.5	490.3	489.6	500.4(4.5)	490.8(9)
c_{44} (GPa)	73.3	112.7	113.3	113.46(6)	113.3(2)
c_{66} (GPa)	39.7	48.7	48.2	48.92(2)	49.0(1)
c_{11}^{iso} (GPa)	305.2	372.7	373.1	381.7	375.0(5)
c_{44}^{iso} (GPa)	74.2	108.7	108.7	109.1	109.3(1)
K (GPa)	206.3	227.8	228.1	236.3	229.3(4)
K_V (GPa)	208.1	230.4	230.8	239.3	232.1(4)
K_R (GPa)	204.5	225.1	225.4	233.3	226.5(4)
$c_{11}{}'^{max}/c_{11}{}'^{min}$	1.47	1.66	1.66	1.66	1.66(1)

* Data revised by Özkan et al., 1974

This is the peer-reviewed, final accepted version for American Mineralogist, published by the Mineralogical Society of America.
The published version is subject to change. Cite as Authors (Year) Title. American Mineralogist, in press.
DOI: https://doi.org/10.2138/am-2023-8986. http://www.minsocam.org/

TABLE 4. Temperature derivatives in MPa/K of the single crystal adiabatic elastic stiffnesses of non-metamict zircon. Error values were derived from fit procedure.

Temperature range	dc_{11}/dT	dc_{12}/dT	dc_{13}/dT	dc_{33}/dT	dc_{44}/dT	dc_{66}/dT	Reference
298 K – 523 K	-45.2	-5.5	-8.6	-43.0	-8.7	-2.3	Özkan, 2008
293 K – 1172 K	-42.6	0.1	-5.5	-36.7	-9.4	-2.0	Ehlers et al., 2022
293 K – 1573 K	-45.36(7)	-2.03(7)	-9.59(7)	-42.85(12)	-9.60(3)	-2.19(1)	This Work

TABLE 5. Fit parameters for double-frequency Einstein model and 4th order polynomial fit of the experimental thermal strain curves. Error values were derived from fit procedure.

Einstein model					
ij	ε_{ij}^{0} (10^{-4} K^{-1})	α_{ij}^{h1} (10^{-6} K^{-1})	Θ_E^1 (K)	α_{ij}^{h2} ($10^{-6}K^{-1}$)	Θ_E^2 (K)
11	-3.25(2)	3.88(1)	1638(3)	1.38(1)	184(6)
33	-5.82(1)	3.49(2)	1837(6)	4.76(2)	476(3)
Polynomial fit (T_0 = 295 K)					
	ε_{ij}^{0} (10^{-6})	α_{ij} ($10^{-6}K^{-1}$)	β_{ij} ($10^{-9}K^{-2}$)	γ_{ij} ($10^{-12}K^{-3}$)	δ_{ij} ($10^{-16}K^{-4}$)
11	-21.9(3)	1.895(2)	3.758(9)	-2.205(14)	4.380(69)
33	-0.5(2)	4.093(1)	4.642(6)	-2.955(10)	7.846(47)

This is the peer-reviewed, final accepted version for American Mineralogist, published by the Mineralogical Society of America.
The published version is subject to change. Cite as Authors (Year) Title. American Mineralogist, in press.
DOI: https://doi.org/10.2138/am-2023-8986. http://www.minsocam.org/

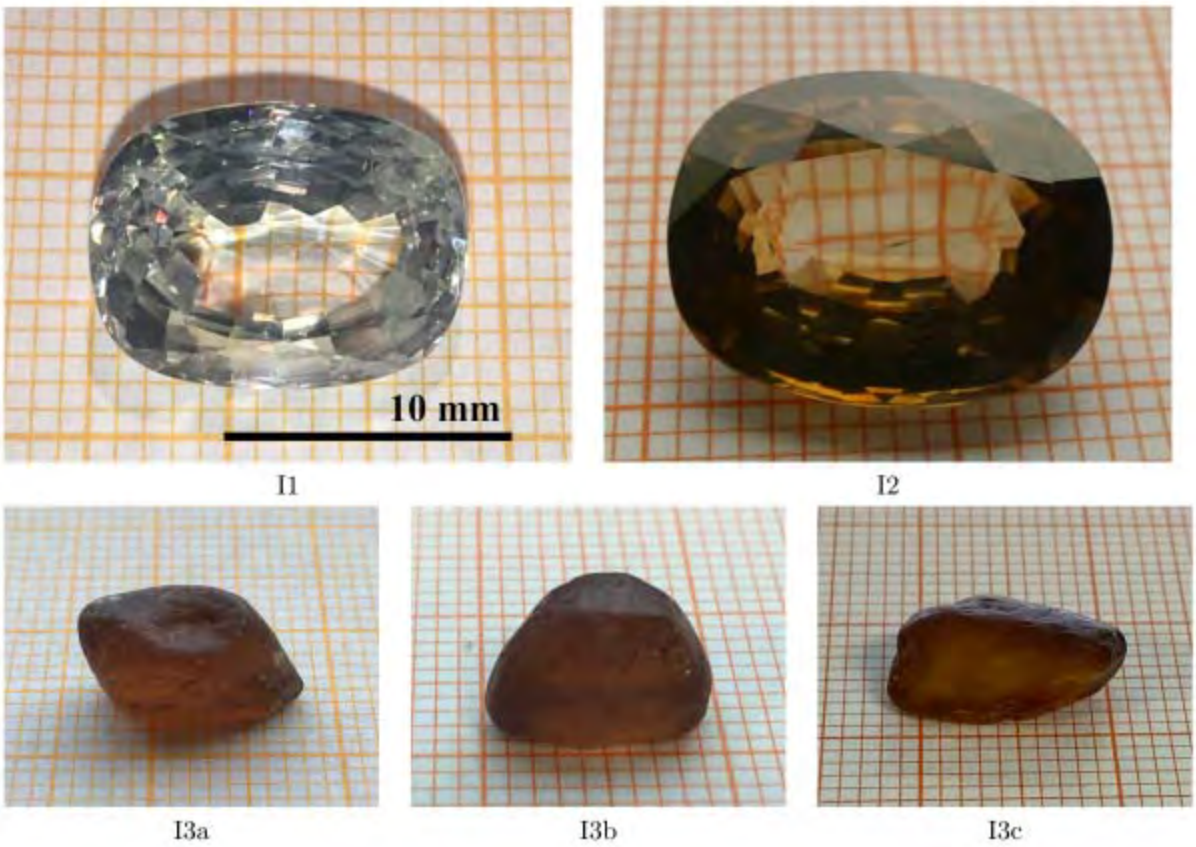

FIGURE 1. Raw crystals used for sample fabrication: I1 (Cambodia), I2 (Sri Lanka), I3a-c (Tanzania).

This is the peer-reviewed, final accepted version for American Mineralogist, published by the Mineralogical Society of America.
The published version is subject to change. Cite as Authors (Year) Title. American Mineralogist, in press.
DOI: https://doi.org/10.2138/am-2023-8986. http://www.minsocam.org/

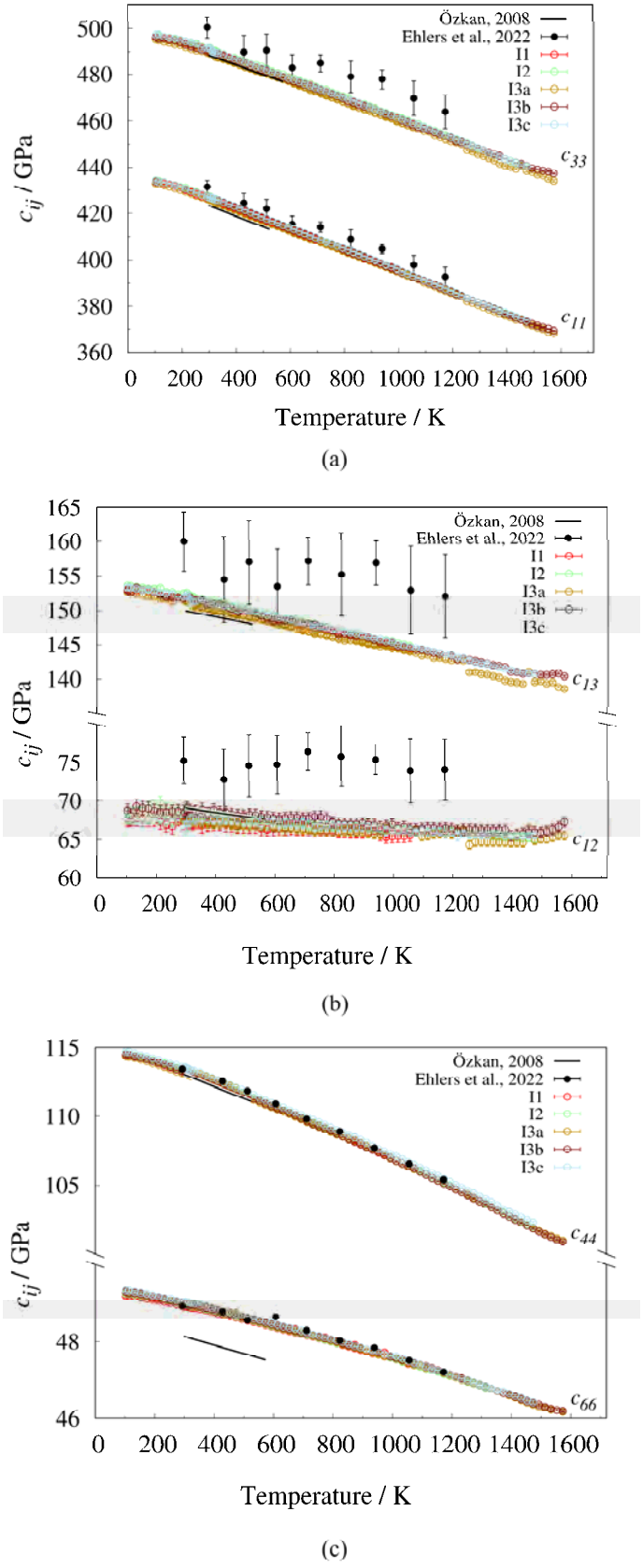

565

FIGURE 2. Temperature-dependence of elastic stiffnesses of non-metamict zircon. (a) longitudinal elastic stiffnesses, (b) transverse interaction coefficients, (c) shear stiffnesses.

This is the peer-reviewed, final accepted version for American Mineralogist, published by the Mineralogical Society of America.
The published version is subject to change. Cite as Authors (Year) Title. American Mineralogist, in press.
DOI: https://doi.org/10.2138/am-2023-8986. http://www.minsocam.org/

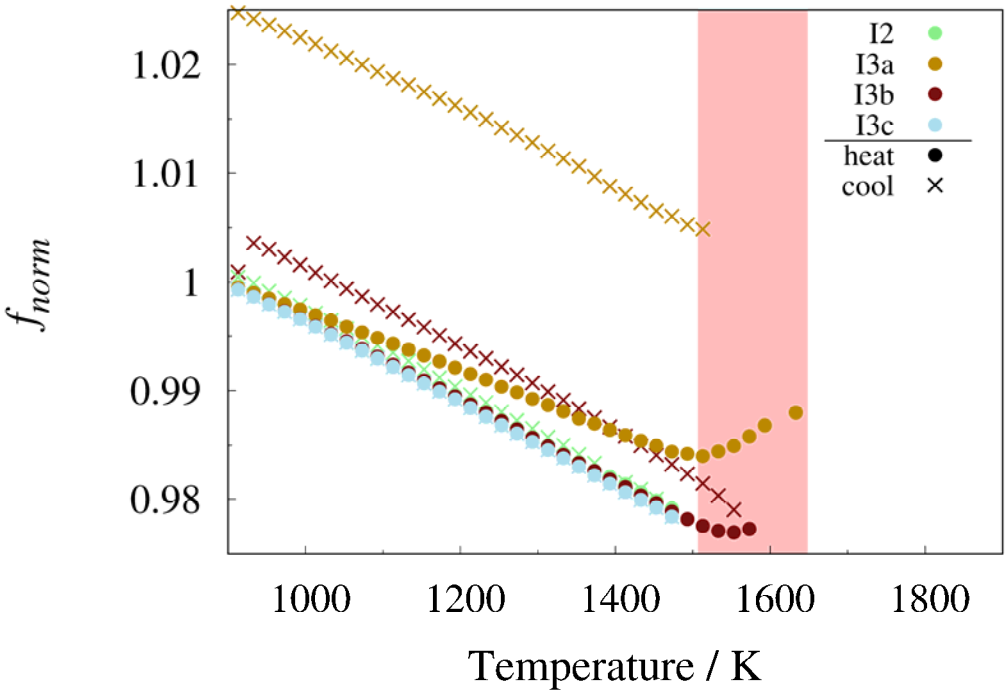

(a)

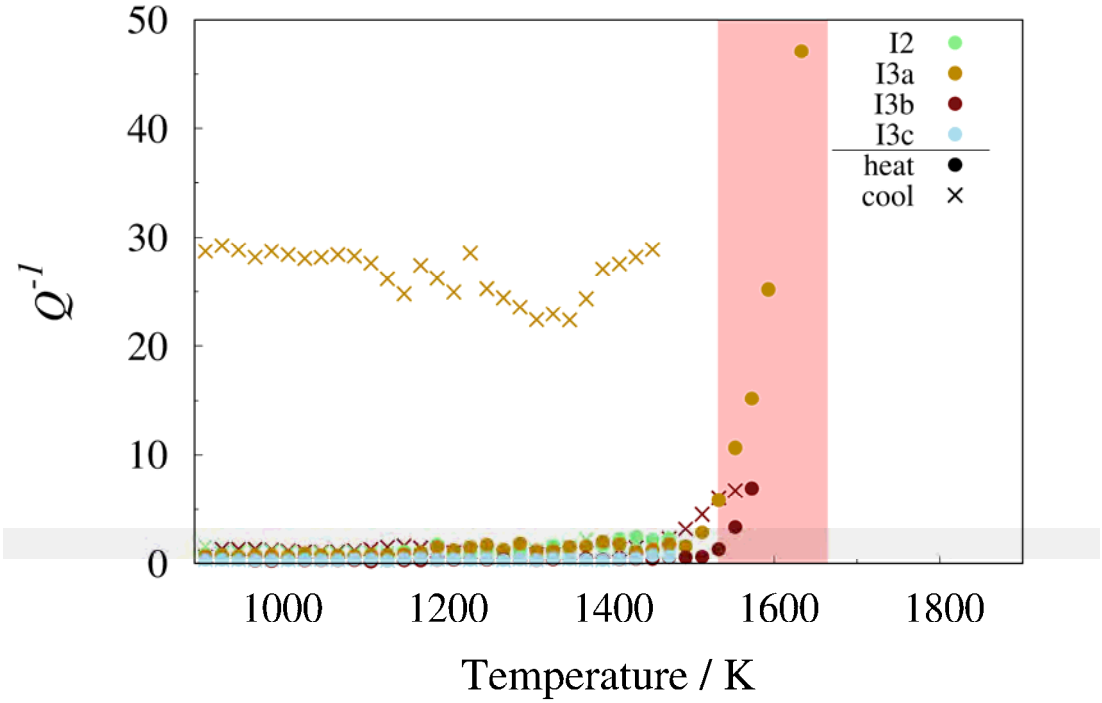

(b)

FIGURE 3. (a) Frequency (normalized to the value at 900 K) and (b) inverse quality factor of a characteristic eigenmode of each sample heated >1450 K.

This is the peer-reviewed, final accepted version for American Mineralogist, published by the Mineralogical Society of America.
The published version is subject to change. Cite as Authors (Year) Title. American Mineralogist, in press.
DOI: https://doi.org/10.2138/am-2023-8986. http://www.minsocam.org/

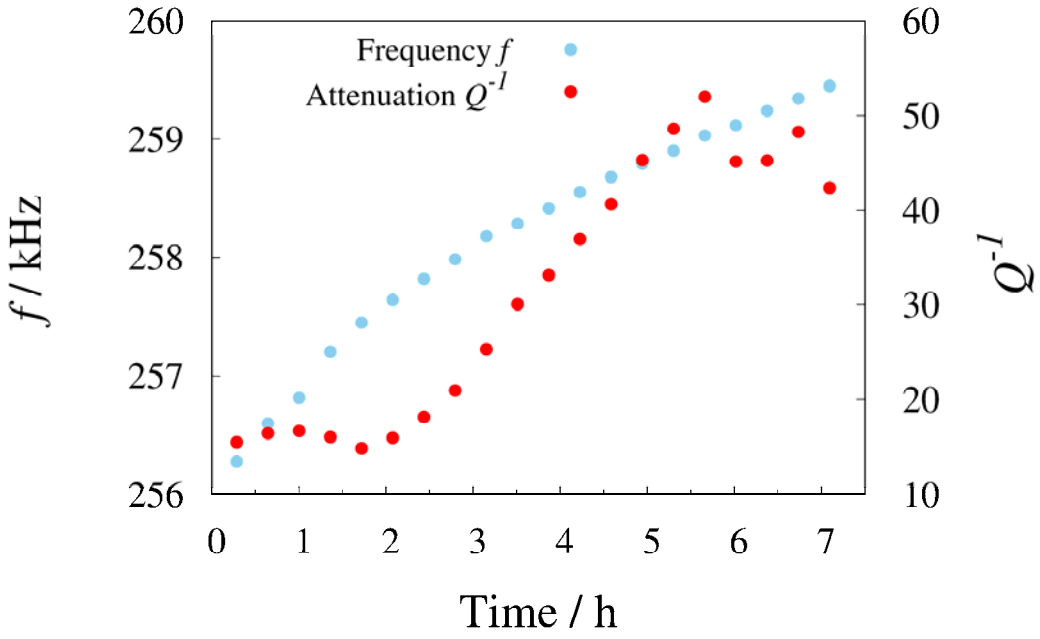

FIGURE 4. Time-dependent change in frequency and inverse quality factor of a selected eigenmode of sample I3a-2 at 1573 K

This is the peer-reviewed, final accepted version for American Mineralogist, published by the Mineralogical Society of America.
The published version is subject to change. Cite as Authors (Year) Title. American Mineralogist, in press.
DOI: https://doi.org/10.2138/am-2023-8986. http://www.minsocam.org/

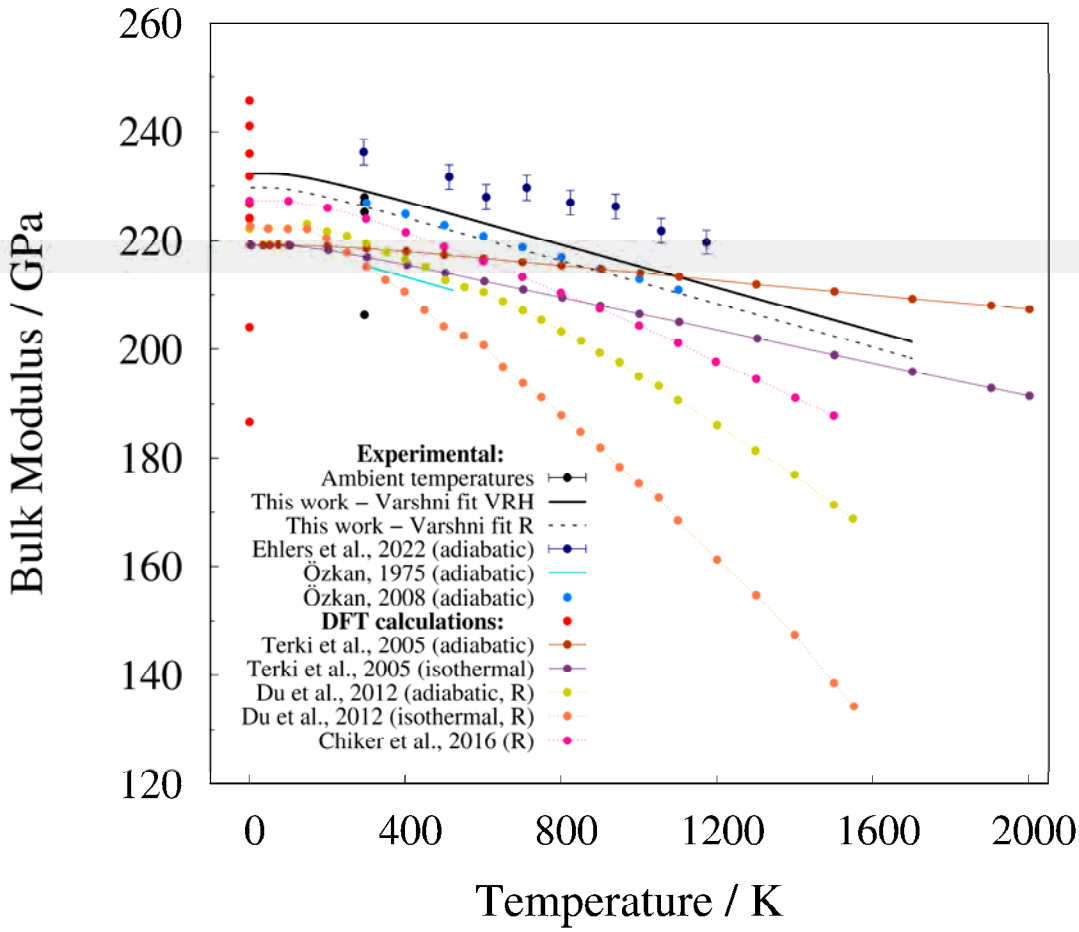

FIGURE 5. Comparison of bulk moduli obtained in this work with published values derived from experimental data as well as from DFT calculations. Temperature-dependent calculations were a combination of DFT and the quasi-Debye model. For citations of published data see text. All values are VRH averages, unless explicitily stated as Reuss modulus by R.

This is the peer-reviewed, final accepted version for American Mineralogist, published by the Mineralogical Society of America.
The published version is subject to change. Cite as Authors (Year) Title. American Mineralogist, in press.
DOI: https://doi.org/10.2138/am-2023-8986. http://www.minsocam.org/

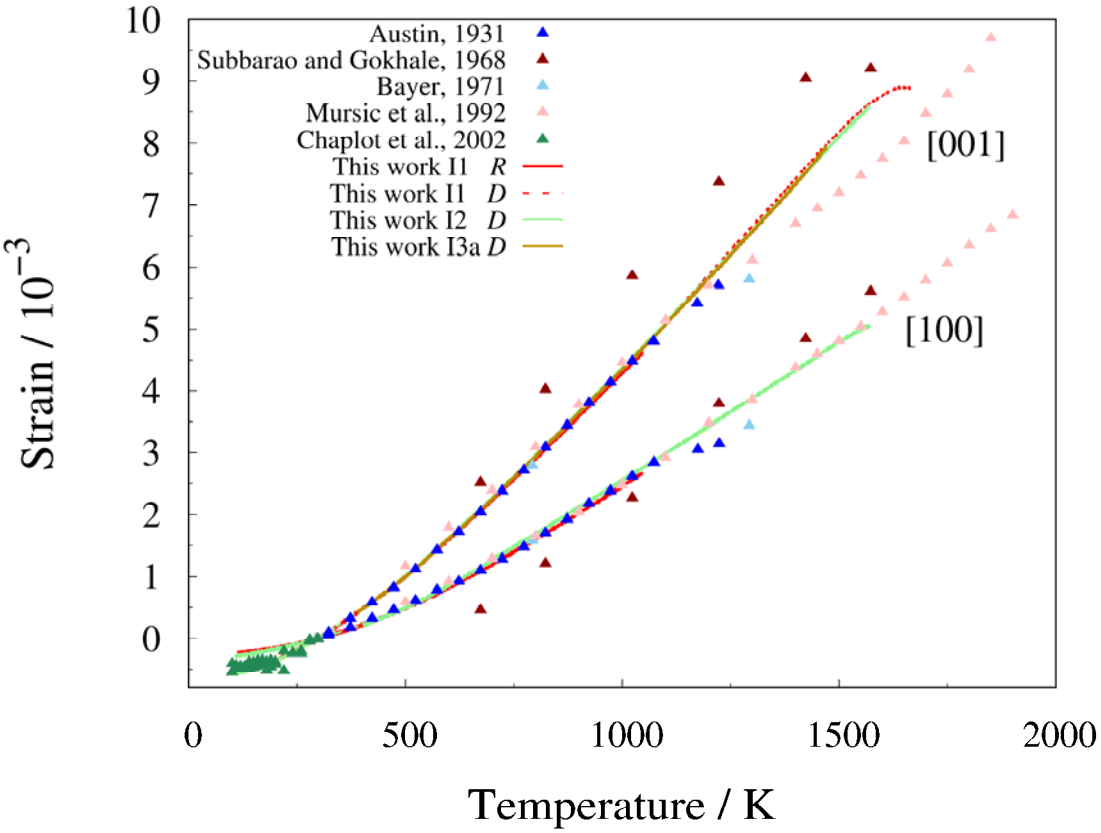

FIGURE 6: Comparison of thermal strains observed on non-metamict zircon samples in this work with corresponding data from literature. *D* denotes initially as-prepared samples, while *R* refers to RUS samples that were previously subjected to high temperatures.

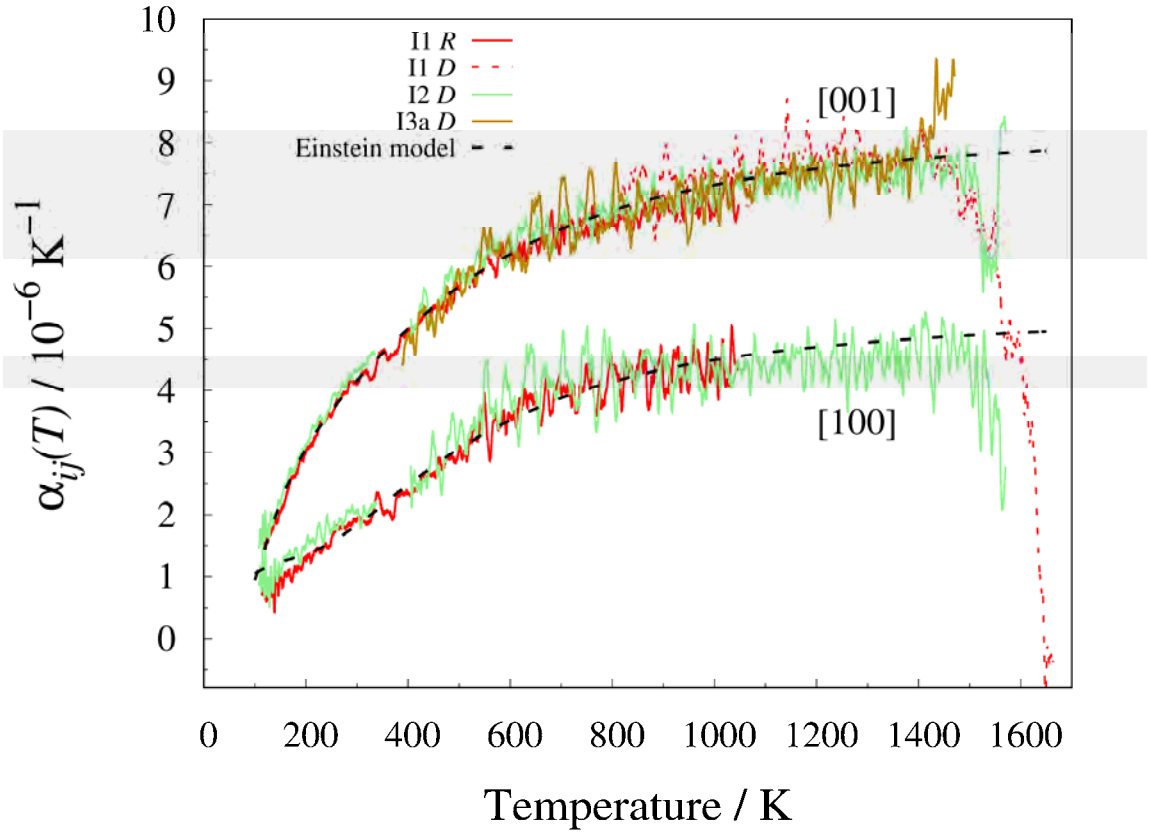

FIGURE 7. Thermal expansion of non-metamict zircon as first derivative of the experimental strain curves (solid lines) obtained in this work and fitted using a double-frequeny Einstein model (dashed lines).

This is the peer-reviewed, final accepted version for American Mineralogist, published by the Mineralogical Society of America.
The published version is subject to change. Cite as Authors (Year) Title. American Mineralogist, in press.
DOI: https://doi.org/10.2138/am-2023-8986. http://www.minsocam.org/

762
763
764
765
766
767
768

769

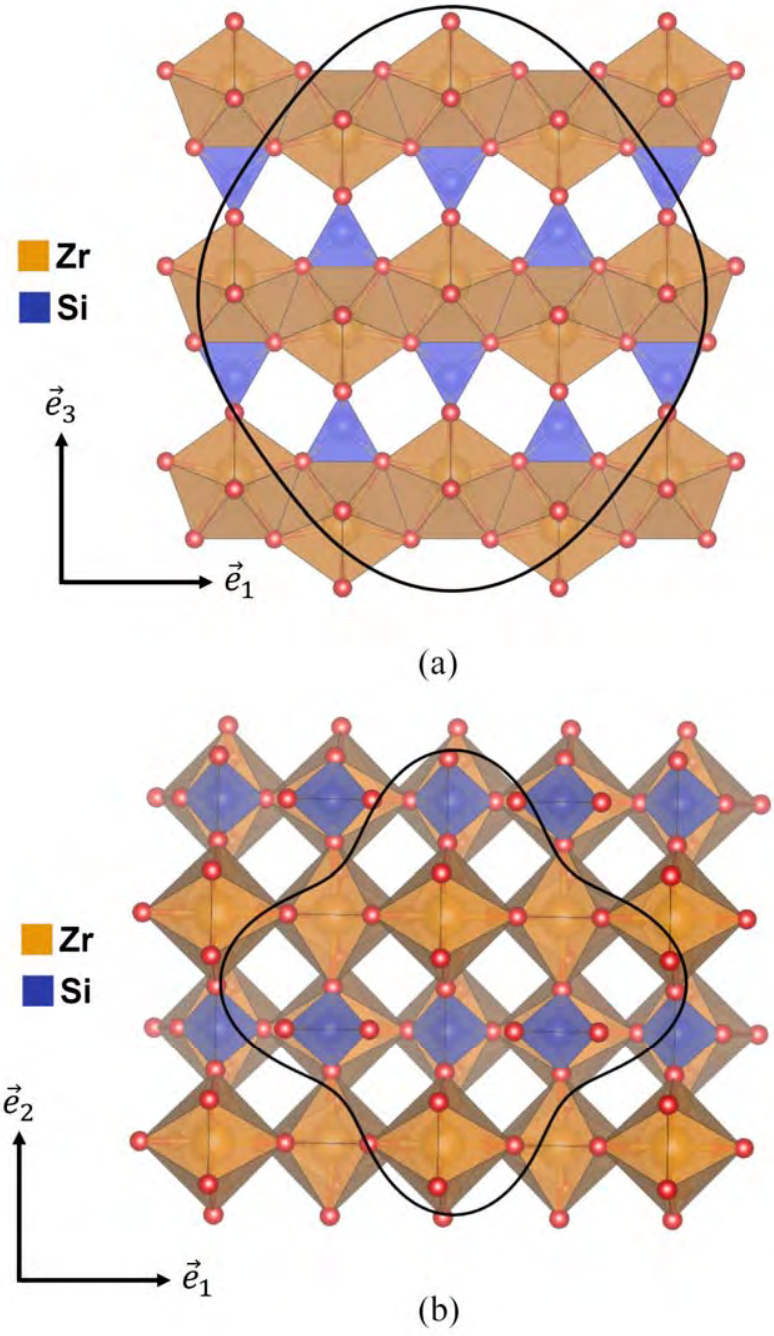

FIGURE 8. Projections of the crystal structure and corresponding cuts of the representation surfaces of the longitudinal elastic stiffnesses c'_{11} for zircon I1 on the plane perpendicular to (a) $\mathbf{e_2}$ and (b) $\mathbf{e_3}$.

This is the peer-reviewed, final accepted version for American Mineralogist, published by the Mineralogical Society of America.
The published version is subject to change. Cite as Authors (Year) Title. American Mineralogist, in press.
DOI: https://doi.org/10.2138/am-2023-8986. http://www.minsocam.org/

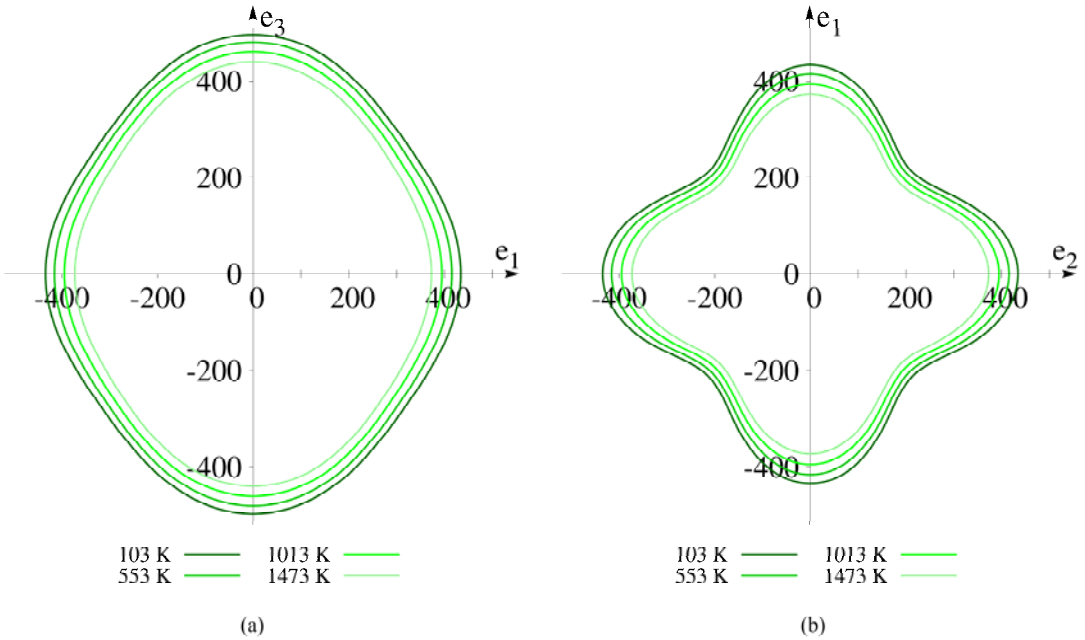

FIGURE 9: Cuts of the representation surfaces of the longitudinal elatic stiffness of zircon I2 at different temperatures perpendicular to (a) $\mathbf{e_2}$ and (b) $\mathbf{e_3}$ (units: GPa).

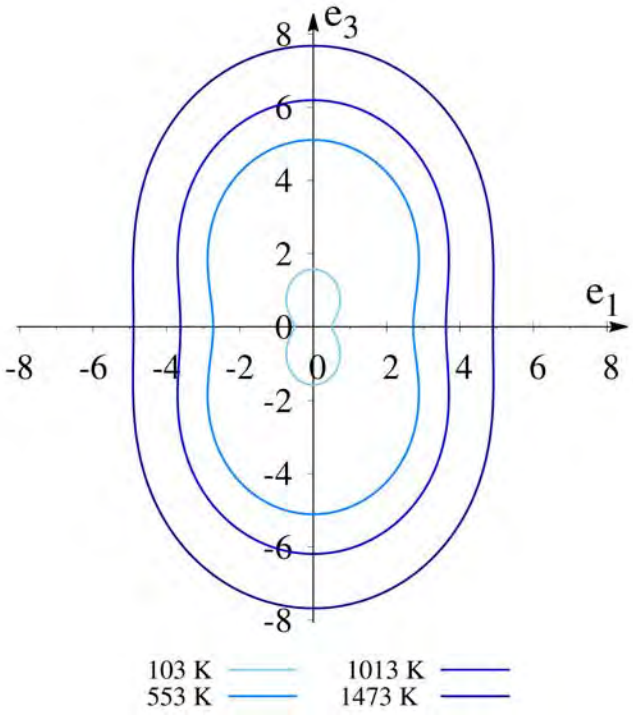

FIGURE 10: Cuts of the representation surfaces of longitudinal thermal expansion of zircon I2 at different temperatures perpendicular to $\mathbf{e_2}$ (units: 10^{-6} K^{-1}).

This is the peer-reviewed, final accepted version for American Mineralogist, published by the Mineralogical Society of America.
The published version is subject to change. Cite as Authors (Year) Title. American Mineralogist, in press.
DOI: https://doi.org/10.2138/am-2023-8986. http://www.minsocam.org/

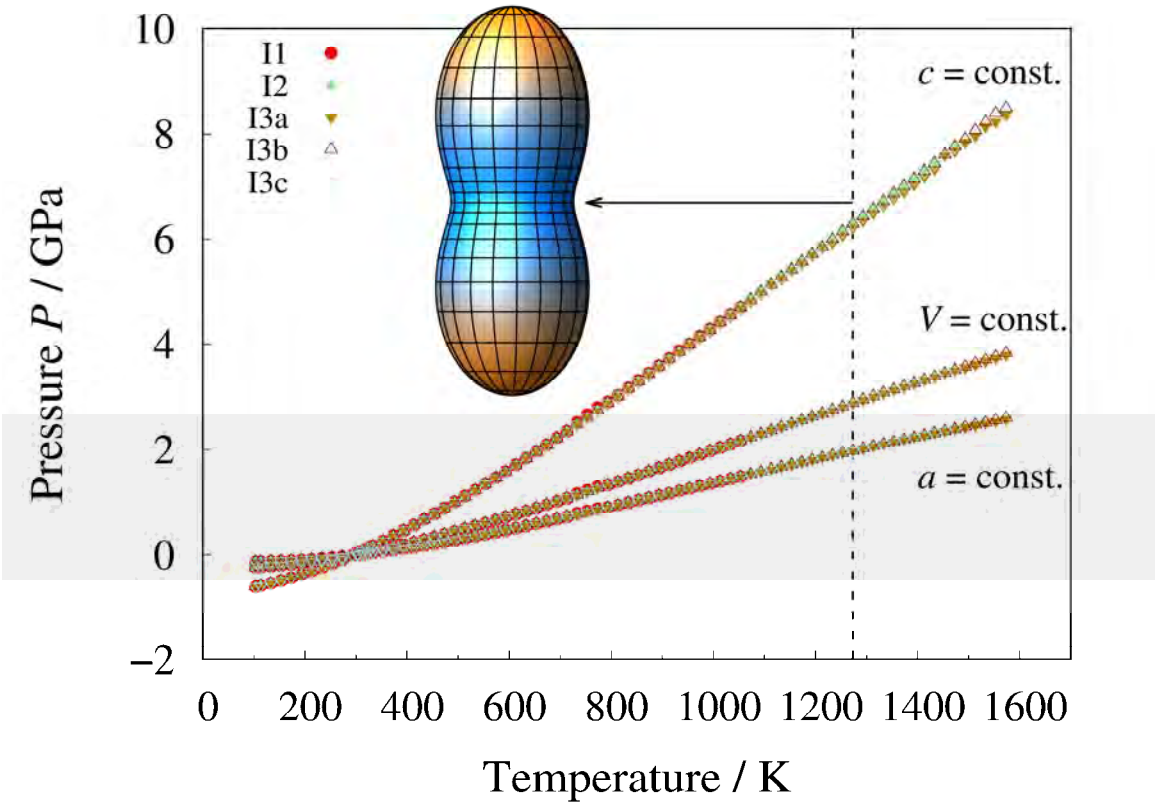

FIGURE 11: Hydrostatic pressure required to compensate effect of thermal expansion on *a* and *c* lattice parameters as well as on volume. The representation surface illustrates the anisotropy of the compensation pressure at 1273 K (tetragonal axis vertical).